LANGMUIR

pubs.acs.org/Langmuir Article

Interplay of Consolidation Fronts and Cracks in Drying Colloidal Coatings and Its Application in Controlling Crack Pattern Formation

Zhaoxia Niu, Han Gao, Masao Doi, Jiajia Zhou, and Ye Xu*

Cite This: *Langmuir* 2022, 38, 13880−13887 Read Online

ACCESS | Metrics & More | Article Recommendations | Supporting Information

ABSTRACT: Cracks are frequently observed in drying colloidal coatings. Although a rich collection of crack patterns has been reported, the systematic study on how cracks grow into the final morphology during the drying process remains elusive. In this work, we use directional drying channels with wedge-shaped edges of different angles to study the interplay of advancing consolidation fronts and propagating cracks. We found that although the shape of the advancing consolidation fronts is altered by the drying edge, the growth direction of the following cracks remains perpendicular to the consolidation fronts during the whole drying process, resulting in cracks with a large curvature. We rationalize the evolution of consolidation fronts with the distribution of capillary pressure revealed by a Laplace model. Further, the growth direction of cracks can be explained by the fracture mechanics mechanism that the main orientation of internal tensile stresses developed during the consolidation determines the crack growth direction. Utilizing this understanding, wavy crack patterns are generated in rectangular drying channels with an alternating temperature field, demonstrating a feasible method of designing and controlling drying-induced crack patterns for micro-/nano-fabrication applications.

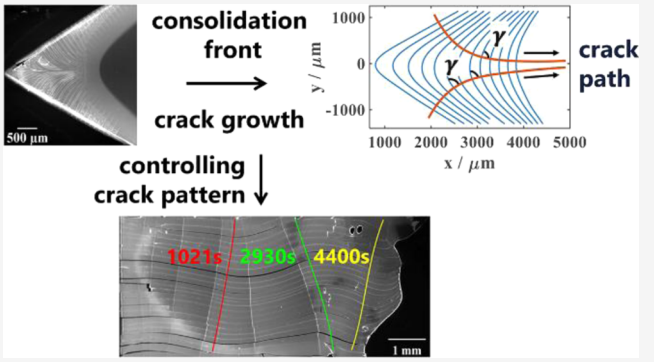

INTRODUCTION

Colloidal particle coatings are widely used in various applications including protective paints,[1] varnishes,[2] photonics crystals,[3] and optical functional coatings.[4,5] These coatings are typically fabricated using a drying process, which transform a complex fluid containing dilute colloidal particles into a solid film with consolidated particles. In this drastic fluid−solid transition, the build-up of internal stresses inside the colloidal coatings can often lead to cracking.[6,7] A rich collection of crack patterns, including circle cracks,[8] arch cracks,[9] wavy cracks,[10] spiral cracks,[11] radial cracks,[12] and strip cracks,[13] have been reported in different colloidal materials under various drying conditions.

Depending on the requirement of particular applications, these drying-induced cracks either should be avoided to prevent the failure of the coating or can be utilized as templates for surface patterns. For protective coatings, many methods, including mixing of hard and soft particles,[14−17] introducing polymeric plasticizers,[18] and sequential deposition of multiple layers,[19,20] have been developed to avoid the cracking for the mechanical and functional integrity. On the other hand, colloidal coatings with well-controlled regular cracks can be utilized as micro-/nano-templates[12,21,22] or microchannels[23] for surface patterns. This approach provides a facile and convenient alternative to conventional micro-/nano-fabrication techniques.[24−27] However, the precise control of crack appearance and propagation remains as a major technical challenge in designing crack patterns on demand.

It is relatively well-understood that the initiation and growth of cracks are closely related to the consolidation of colloidal particle coatings during the drying process. In the consolidated region, where colloidal particles become closely packed upon drying, in-plane tensile internal stress can be built up due to the compression by the capillary pressure and the constraint of the solid substrate. Once the internal stress exceeds the critical value, it will result in the cracking of colloidal coatings.[28,29] It has been reported that cracks usually propagate in an intermittent manner with the crack tips following the advancing consolidation front, which is the boundary between the consolidated and dilute regions, with a sharp gradient in the volume fraction of colloidal particles.[13] It has also been observed that the path of crack growth can be affected by the shape of consolidation fronts.[22,30] In a few early studies, the shape of cracks has been related to the orientation of the internal stress tensor or the direction of the maximum energy release rate.[10,31] However, a direct correlation

Received: August 3, 2022
Revised: October 21, 2022
Published: November 3, 2022

https://doi.org/10.1021/acs.langmuir.2c02088
Langmuir 2022, 38, 13880−13887

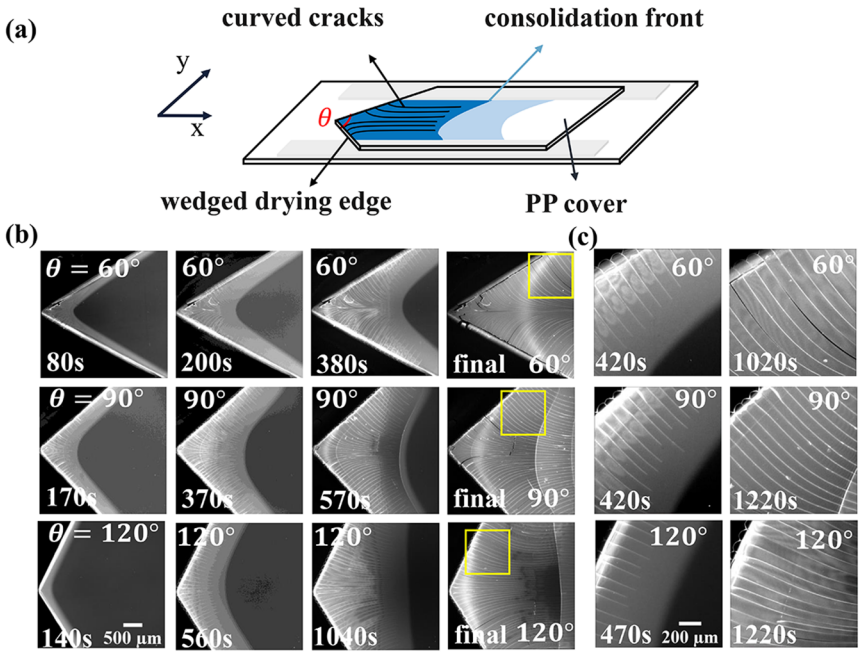

Figure 1. Observation of the advancing consolidation fronts and cracks in directional drying setups with angled drying edges. (a) Schematic of the directional drying experiment setup with a wedge-shaped drying edge. The origin of the coordinate system is set at the tip of the angled drying edge, and the directions are indicated by the arrow. (b) Fluorescence microscopy images at different drying times with three drying edges of angles $\theta = 60°$, $\theta = 90°$, and $\theta = 120°$, respectively. (c) Magnified images of the yellow boxes of (b) at different drying times for three drying edges of angles $\theta = 60°$, $\theta = 90°$, and $\theta = 120°$, respectively.

between the morphology of consolidation fronts and cracks has still not been systematically investigated.

Herein, we use a directional drying setup with wedge-shaped drying edges to study the drying and cracking processes of colloidal suspensions. The morphologies of advancing consolidation fronts and the crack patterns are quantified for wedge edges of different angles to study the effect of the drying boundary. The experimental results are also correlated with the Laplace model, using which the distribution of water pressure is calculated. By analyzing the geometrical relations between the crack growth path and evolution of the consolidation front, we propose that the principal direction of the internal stress tensor developed during the consolidation is responsible for the direction of crack propagation. Based on these understandings, we utilize a temperature gradient to control the direction of drying-induced cracks and generate wavy crack patterns in a straight drying channel. Our work demonstrates the feasibility of designing and controlling crack patterns for potential micro-/nano-fabrications.

EXPERIMENTAL SECTION

Colloidal Suspension. Aqueous suspensions of monodisperse colloidal silica nanoparticles (LUDOX AS-40) were purchased from Sigma-Aldrich. The particle diameter is about 24 ± 3 nm, and the size distribution is shown in Figure S1. The initial concentration is 40 wt % (~22 vol %). About 0.2% yellow−green fluorescent particles (0.1 μm, carboxylate-modified, Molecular Probes) were added to the suspension to enhance the contrast and facilitate visualization when observed under the fluorescence microscope. The addition of the fluorescent particle in the colloidal silica suspension has no visible effect on the crack patterns, as shown in Figure S2. The prepared dispersion was then put in an ultrasonic bath for 5 min to ensure thorough mixing.

Setup and Methods. The directional evaporation setup is shown in Figure 1a. The glass slides are cleaned ultrasonically with ethanol for 30 min and then dried in a clean stream of nitrogen to remove any residual ethanol. For the preparation of different drying edges, polypropylene (PP) sheets (a thickness of about 300 μm) are cut into wedge-like shapes with different angles (60, 90, 120, and 180°) on one of the sides. The PP cover and the glass slide are then attached together using two strips of spacers, resulting in a thin channel with a height of 80 μm, a width of 4 mm, and a length of 40 mm. We exploit the capillary force to load the colloidal suspension into the channel from the angled edge. After that, the samples are kept in a clean room with the temperature of 22 °C and the humidity of 50% until the solvent is fully evaporated. During the drying process, the colloidal suspension inside the channel is observed using an inverted microscope (Eclipse Ti2-E, Nikon) with a 4× objective lens (NA = 0.13) under blue fluorescent light (FITC filter). The whole drying process is recorded at 1 s intervals using a digital camera (Prime BSI, Photometrics). The individual field of view (FOV) is approximately 3.3 × 3.3 mm^2 with the pixel size of 1.62 μm. The features shown in the recorded images are extracted and analyzed using the image processing toolbox of MATLAB software. For all the analyses in this work, the coordination system is shown in Figure 1a, and the origin is set at the tip of the angled drying edge.

RESULTS AND DISCUSSION

Morphology of Consolidation Fronts and Cracks. The drying process and evolution of cracking in channels with different drying edges are recorded and analyzed as shown in Figure 1b,c. After the colloidal suspension starts drying from the filling end, the evaporation of water drives the colloidal particles to pack and consolidate continuously on the angled drying edge, where the three-phase contact line is pinned. The region with consolidated particles appears much brighter due to the increased concentration of fluorescent particles, and this consolidation region continues to grow during the drying process, as shown in Figure 1b. The consolidation front, defined as the boundary between the consolidated and fluid regions, evolves from a shape that mimics the wedge-shaped drying edge into a straight line as it advances smoothly into the channel. Closely following the advances of the consolidation front, an

https://doi.org/10.1021/acs.langmuir.2c02088
Langmuir 2022, 38, 13880−13887

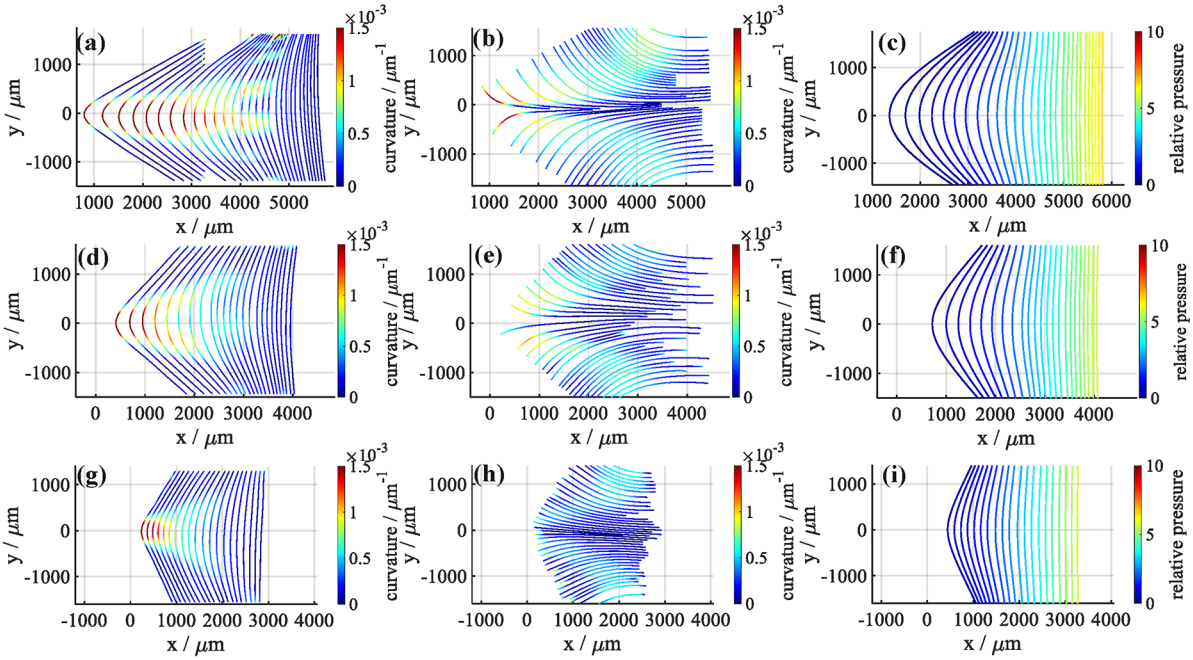

Figure 2. Comparison of consolidation fronts and cracks extracted from experiments with equal pressure lines from the Laplace model. (a,d,g) are extracted consolidation fronts in the angled drying channel θ = 60, 90, and 120°, respectively, at different drying times. The time increases gradually from right to left with an interval of 60 s. The color bar represents the curvature of the consolidation fronts. (b,e,h) are extracted final crack patterns in the drying channel with the drying edge θ = 60, 90, and 120°, respectively. The color bar represents the curvature of the cracks. (c,f,i) are equal pressure lines solved from the Laplace models of angled drying edges of θ = 60, 90, and 120°, respectively. The color bar represents the relative pressure.

array of cracks occurs and continuously grows toward the newly formed consolidation region. For all three setups with wedge-shaped drying edges, cracks first appear as two arrays of parallel lines perpendicular to the drying edge, similar to those observed in directional drying setups.[32,33] As cracks initiated from two sides of the angled drying edges grow into each other, the cracks start to deviate from straight lines into curved paths, as if they would like to avoid crossing each other. These two arrays of crack eventually emerge into a single array of parallel straight lines. The curved paths of propagating cracks are shown in the magnified images in Figure 1c.

To quantify the evolution of consolidation fronts and cracks, we extract the consolidation fronts at various drying stages and the final crack pattern from the micrographs recorded during the drying process. These extracted profile lines of consolidation fronts and cracks are fitted into polynomial functions to calculate the curvature at each location. The profiles and local curvature for consolidation fronts and cracks are shown in Figure 2a,d,g and b,e,h, respectively. As an example, Figure 2a shows a series of consolidation fronts, recorded at a time interval of 60 s, with the local curvature color-coded. Due to the sharp 60° angle of the drying edge, the consolidation fronts at the early stage exhibit a large curvature, particularly in the center of the drying channel. With the advance of the consolidation front, its curvature gradually decreases until it becomes almost a straight line. The evolutions of the consolidation fronts in drying channels with 90 and 120° drying edges show similar trends, as shown in Figure 2d,g. Because of the larger angles at the drying edges, the curvature of the consolidation fronts in those two setups appear smaller at the initial stages. The curvature of cracks are also affected by the angled drying edges, as shown in Figure 2b,e,h. Similar to those of consolidation fronts, the maximum curvature shown in cracks also increase with the sharpening of the wedge-shaped drying edge. The maximum curvature of both consolidation fronts and cracks for different drying edges are shown in Figure S3. In addition, the dynamic evolution of consolidation fronts and the propagation of cracks in drying channels with different angled edges can be found in Movies S1, S2, and S3 in the Supporting Information.

Our experimental results show that the evolution of consolidation fronts and final crack patterns are affected by the angled drying edges. This finding is similar to the observations reported in an earlier study that investigated the crack patterns in silica suspensions dried in channels with multiple openings.[10,34] In order to better understand the evolution of consolidation fronts in drying setups with angled drying edges, we develop a theoretical model to understand the flow and pressure distribution in directional drying setups with angled edges as the boundary conditions for evaporation. In the region between the consolidation front and the drying edge, the colloids are nearly close-packed, and the water fraction remains almost constant.[13] The transport of the water to the drying edge is due to the pressure difference induced by evaporation. At the drying edge, the pressure is negative due to the concave shape of the meniscus formed among solid particles, $P_c = -\frac{2\gamma}{r_M}$, where r_M is the radius of curvature of the meniscus. For close-packed spheres, this can be as small as the minimum pore radius, $r_M^{min} \approx 0.15a$ (a is the radius of particles). On the solution side, the pressure is constant along the consolidation front, and its value is almost zero with the atmosphere pressure, as given in ref 32. The water flow is given by Darcy's law

$$\boldsymbol{J} = -\frac{k}{\eta}\nabla P \tag{1}$$

where k is the permeability depending on the colloidal fraction and η is the viscosity of water. Inside the drying channel except the drying edge, the volume of water is conserved; therefore, we

https://doi.org/10.1021/acs.langmuir.2c02088
Langmuir 2022, 38, 13880−13887

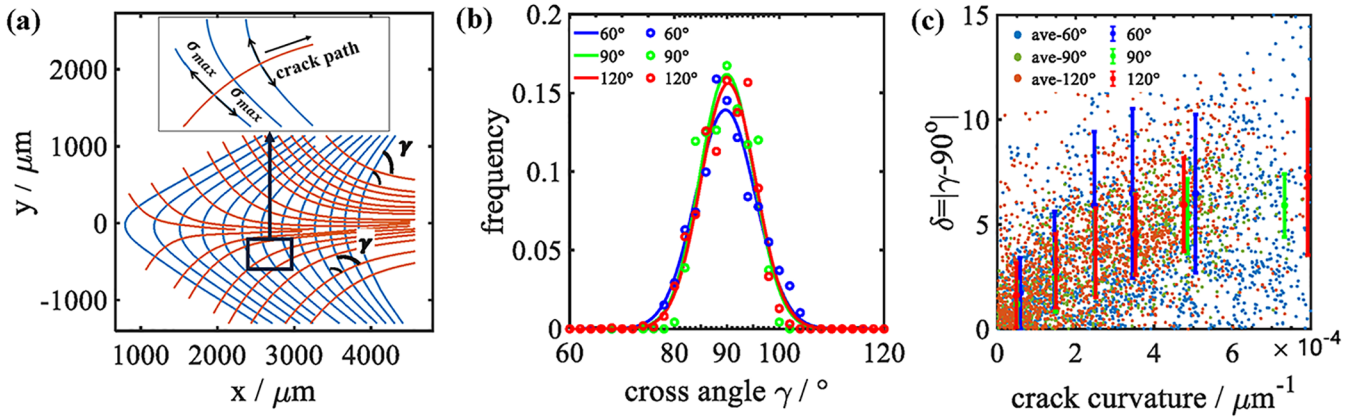

Figure 3. Statistics of cross angles between the consolidation fronts and cracks. (a) Overlay of consolidation fronts at a time interval of 60 s and the final crack pattern with the drying edge of angle $\theta = 60°$. γ marks the cross angles between the consolidation fronts and cracks. The inset is the schematic of the internal stress and crack growth paths. (b) Statistic frequency of cross angles γ with different drying edges ($\theta = 60$, 90, and 120°) (circle points) and the corresponding Gaussian fitting distribution (solid lines). (c) Deviation of the cross angle γ from 90° vs the local curvature of the cracks (scatter points: blue, green, and red for drying edges of angles $\theta = 60$, 90, and 120°, respectively) and mean values and standard deviations over a range of curvature of 1×10^{-4} μm^{-1} (error bar lines: blue, green, and red for drying edges of angles $\theta = 60$, 90, and 120°, respectively).

have $\nabla \bullet \boldsymbol{J} = 0$. Since the colloidal fraction is almost constant in the solid region, the permeability is also constant; therefore, the pressure satisfies the Laplace equation

$$\nabla^2 P = 0 \tag{2}$$

Ideally, one needs to solve the Laplace equation in the solid regions for every instance, then update the consolidation front for the next time step based on the pressure gradient at the boundary, and repeat this process to obtain the time evolution of the consolidation front. Alternatively, since the consolidation front is also an equal-pressure line, one might solve the Laplace equation with fixed boundary conditions (one at the evaporation front and the other at the far away solution side), and the equal-pressure lines of the solution correspond to the consolidation front at different times. The exact time that one specific equal-pressure line corresponds to can be calculated from the evaporation rate (Figure S4). These equal-pressure lines with different angled drying edges in Figure 2c,f,i also evolve from the arrow-like shape to nearly straight lines, which display a similar morphology to the consolidation fronts in Figure 2a,d,g. This comparison shows that the angled drying edge can affect the pressure distribution of water inside the drying channel, which will in turn affect the evolution morphology of consolidation fonts.

Geometrical Relation between the Crack Growth Direction and Consolidation Fronts. To better understand the interaction between the consolidation fronts and the cracks, we further quantify the relationship of the growth direction of cracks and profiles of consolidation fronts. As an example, the extracted consolidation fronts at the time interval of 60 s (blue lines) and the final crack pattern (red lines) in the drying channel with the 60° angled drying edge is shown in Figure 3a. The cross angle, γ, between the growth direction of the crack and the consolidation fronts can be then extracted from these two sets of lines, as marked in Figure 3a. The statistical results of about 1200 measurements of cross angles, together with those extracted from the samples with 90 and 120° angled drying edges, are shown as the histogram in Figure 3b, and the data of each drying edge are fitted by a Gaussian distribution. Despite the different appearances of crack patterns, the distributions of extracted cross angles for the three different drying setups are all centered at 90° with very similar distributions. The mean values and standard deviations of the three sets of angles are 89.1° ± 6.2°, 90.7° ± 4.2°, and 90.0° ± 4.6°, respectively. This means that the cracks have a strong tendency to be perpendicular to the consolidation front, even if this requires changing propagation directions.

From the distribution shown in Figure 3b, we notice that there remains still a fraction of measured cross angles that deviate from 90°. We hypothesize that these deviations are related to the part of cracks with a high curvature. Therefore, we quantify these deviations, $\delta = |\gamma - 90°|$, and plot these values versus the local curvature of the cracks where the cross angle was measured. These scattered data points are then averaged over a range of curvature of 1×10^{-4} μm^{-1}, and the mean values and standard deviations are plotted as the error bar lines in Figure 3c. The results for all three drying channels with different angled edges exhibit the same trend that δ increases with the curvature of cracks. This trend is also confirmed by correlating the evolution of δ and the local curvature of individual cracks as they grow (Figures S5−S7 in the Supporting Information). These results suggest that while the cracks tend to grow along the direction perpendicular to the consolidation front, they appear to increasingly deviate from this direction when they are already heavily curved.

The relationship between the consolidation front and propagating cracks can be understood from the spatial distribution of capillary pressure and the fundamentals of fracture mechanics. During the directional drying of colloidal suspension, water flows continuously to the drying edge to replenish that lost by evaporation.[13] This convection flow deposits and compacts the colloidal particles near the drying edge, resulting in a growing area of the consolidated region. The capillary force further compacts the consolidated particle network, which leads to the accumulation of tensile stresses inside the colloidal coating. When the accumulated stress exceeds the fracture limit of the colloidal coating, the quasistatic cracks will start to grow intermittently and follow closely behind the moving consolidation front.[35] As reported in previous studies, the water pressure gradient is closely related to the distribution of internal stresses developed in the consolidated region.[10,36] Specifically, the direction of the maximum tensile

https://doi.org/10.1021/acs.langmuir.2c02088
Langmuir 2022, 38, 13880−13887

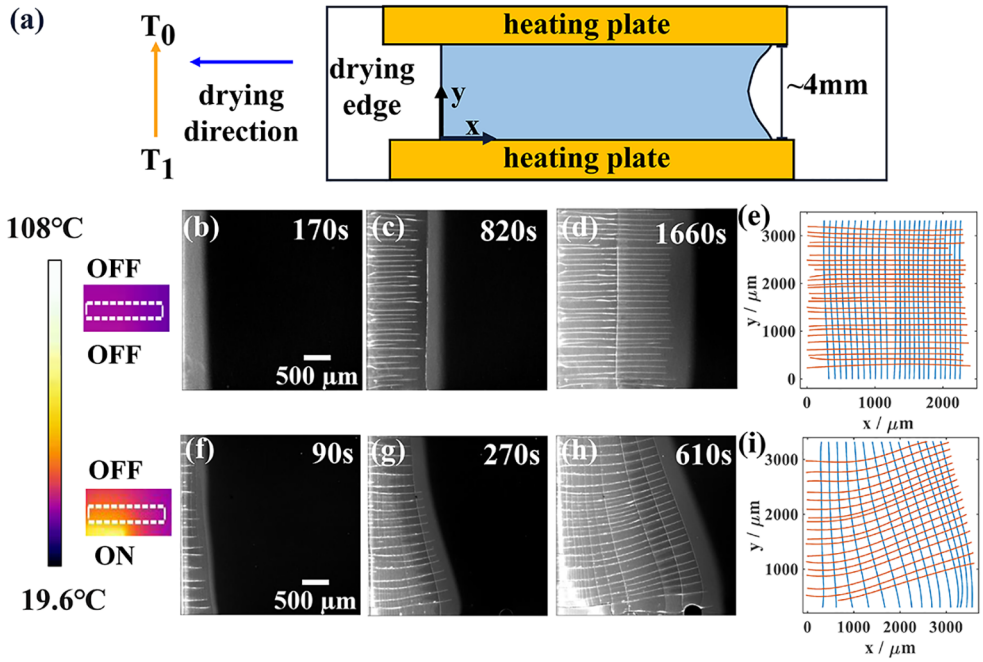

Figure 4. Controlling advancing consolidation fronts and crack patterns with a temperature gradient. (a) Schematic of the directional drying experimental setup with the tunable temperature field. (b–d) Fluorescence microscopy images at different drying times with a uniform temperature field. (e) Extracted consolidation fronts at different times at the interval of 60 s and the final crack pattern of the uniform temperature field. (f–h) Fluorescence microscopy images at different drying times with a gradient temperature field created by turning on the top heating plate. (i) Extracted consolidation fronts at different times at the interval of 60 s and the final crack pattern of the gradient temperature field. Snapshots of thermal infrared images to the left of (d,f) are also shown for the uniform temperature field (top) and the gradient temperature field (bottom), respectively. The white dashed boxes indicate the location of the drying channel.

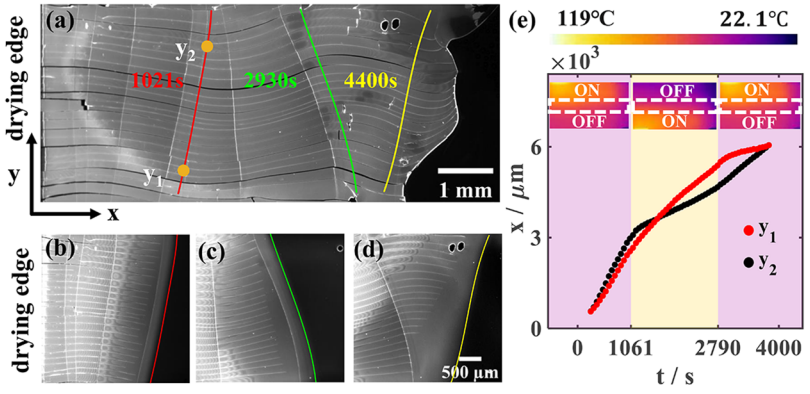

Figure 5. Generation of wavy crack patterns with alternating temperature gradients. (a) Fluorescence microscopy image of the final wavy cracks. The red, green, and yellow lines represent the positions of the consolidation front at drying times of t = 1021 s, t = 2930 s, and t = 4400 s, respectively. (b–d) In situ fluorescence microscopy image during the formation of wavy cracks at drying times of t = 1021 s (e), t = 2930 s (d), and t = 4400 s (c), respectively. The color of consolidation fronts is consistent with that in (a). (e) Evolution of the x position vs the drying time of the two positions of consolidation fronts: y_1 and y_2 [yellow point shown in (a)]. The thermal infrared images represent the ON/OFF state of the heating plates on both sides of the channel at three different time periods. The location of the drying channel is indicated with the white dotted lines.

stress, σ_{max}, is perpendicular to the direction with the gradient of the water pressure, as shown in Figure 3a. In our experimental setups, the angled wedge-shape edge affects the water pressure distribution and the shapes of the consolidation fronts inside the drying channel, as shown in Figure 2c,f,i. This suggests that the direction of the maximum internal stress is parallel to the consolidation front and perpendicular to the gradient of the water pressure. According to the principle of fracture mechanics, the crack will propagate in the direction perpendicular to the direction of maximum tensile stress.[9,31] Therefore, the cracks in the drying colloidal coatings grow along a path perpendicular to the consolidation fronts, which results in curved crack patterns that are not commonly observed in failed materials.

Guiding the Crack Growth Direction by Controlling the Advancing Consolidation Fronts. Based on the analysis about the correlation between the consolidation front and the propagation direction of cracks, we explore the approach for controlling the crack pattern by changing the morphology of the consolidation front. We modify our drying channel by adding two strips of ceramic heating plates to each side of the channel. These two heating plates can be individually controlled to generate a temperature gradient along the y-direction near the

https://doi.org/10.1021/acs.langmuir.2c02088
Langmuir 2022, 38, 13880–13887

drying edge, as shown in Figure 4a. The temperature distribution across the drying channel is recorded using an infrared camera (FLIR T420 IR) and is shown in Figure 4. A temperature gradient in the range of 5 ± 3 °C/mm can be established by this asymmetric heating.

The consolidation fronts and cracks can exhibit distinct morphologies with a uniform temperature field or gradient temperature fields. For experiments at a uniform temperature gradient without heating plates, the consolidation front form and advance parallel to the flat drying edge (θ = 180°) in the drying channel, followed by an array of cracks that grow in the direction perpendicular to the consolidation front, as shown in Figure 4b−e. However, when one heating plate is turned on, resulting in a temperature gradient near the drying edge, the consolidation front advances faster on the side with the higher temperature due to the higher evaporation rate. This uneven evaporation leads to the deflection of the consolidation front that is no longer parallel to the drying edge. During this process, the deflection angle of the consolidation front (β, as shown in Figure S9) gradually increases and then remains stable at around 20°. The statistical frequency of cross angles between consolidation fronts and cracks in the two temperature fields in Figure S8 shows a very narrow distribution. As a result, cracks also change their propagation direction to remain perpendicular to the consolidation fronts, as shown in Figure 4f−i.

Furthermore, more complex wavy crack patterns can be achieved by varying the temperature gradient near the drying edge, as shown in Figure 5a. We alternate the "on" and "off" states of two heating plates, and the temperature distribution of different states is shown in the thermal infrared image in Figure 5e. Different colors of the background in Figure 5e indicate different stages of heating. The morphology of consolidation fronts and cracks in response to the temperature gradient in every state is shown in Figure 5b−d. When the bottom heating plate is off and the top one is on at the beginning of the drying process, the consolidation front line rotates clockwise and the array of cracks deflect downward in response to the temperature gradient. At t = 1061 s, we turn on the bottom heating plate and turn off the top one, resulting in a temperature gradient with the opposite direction. Soon after that, the consolidation front rotates counter-clockwise and the cracks deflect upward. After alternating the temperature gradient for three times, an array of wavy cracks are successfully generated in Figure 5a. The advancing position x of consolidation fronts in the drying process at different y-positions in Figure 5e shows the morphology deflection process of the consolidation fronts. The movie and the photo of the whole drying process with alternating temperature gradients can also be found in the Supporting Information (Movie S4 and Figure S10). This generation of wavy crack patterns demonstrates the feasibility of designing and producing complex crack patterns by controlling the evolution of consolidation fronts, which can be achieved by applying other external fields to modify evaporation rates. By utilizing the dependence of the crack propagation on the advancing consolidation fronts, we are potentially able to customize the morphology of drying-induced cracks, which can be used for micro-/nano-fabrications. For example, the cracks of colloidal coatings can be used as the templates for a metal conductive grid,[21] the microchannels for supramolecular structures,[37] and a method to obtaining the centimeter-scale rods assembled by colloidal particles.[22] With a better control of the growth path of cracks, more complex crack patterns can be generated and used in these micro-/nano-fabrication applications.

CONCLUSIONS

In summary, we employ a directional drying channel setup with wedge-shaped drying edges of various angles to investigate the intriguing interaction between the consolidation of colloids and the following cracks. We found that the drying edge can affect the morphologies of consolidation fronts, and this phenomenon is explained by a Laplace model built for water pressure distribution inside the drying channel. Moreover, the measurements of cross angles between the consolidation front and the cracks clearly show that the cracks tend to grow in the direction perpendicular to the consolidation front, in spite of the slight deviation of this geometrical relation for cracks with a high curvature. By combining experimental observation and theoretical modeling, we propose that the orientation of the main tensile internal stress developed near the consolidation front determines the direction of crack propagation. This finding is within the framework of fracture mechanics and is also consistent with other observations of complex crack patterns in different colloidal systems.[9,10,31] Based on this understanding, we utilize the effect of the gradient temperature field on the morphology evolution of the consolidation front to control the growth path of cracks and produce an array of wavy cracks inside a rectangular drying channel. Our crack control strategy provides a new direction to design and produce specific crack patterns, which can potentially be applied in the micro-/nano-fabrication field.

ASSOCIATED CONTENT

Supporting Information

The Supporting Information is available free of charge at https://pubs.acs.org/doi/10.1021/acs.langmuir.2c02088.

Detailed description about the colloidal suspension used in this work; supplementary analysis of the morphology of consolidation fronts and cracks; geometrical relation between the growth direction of individual cracks and consolidation fronts; and additional analysis on guiding the crack growth direction by controlling advancing consolidation fronts (PDF)

Time-lapse video of fluorescence images of consolidation fronts and cracks in directional drying channels with a drying edge of angle θ = 60°, which is shown accelerated by 240 times (AVI)

Time-lapse video of fluorescence images of consolidation fronts and cracks in directional drying channels with a drying edge of angle θ = 90°, which is shown accelerated by 240 times (AVI)

Time-lapse video of fluorescence images of consolidation fronts and cracks in directional drying channels with a drying edge of angle θ = 120°, which is shown accelerated by 240 times (AVI)

Time-lapse fluorescence images recorded during the formation of wavy cracks in directional drying channels with alternating temperature gradients, for which the movie is accelerated by 480 times (AVI)

AUTHOR INFORMATION

Corresponding Author

Ye Xu − *School of Mechanical Engineering and Automation, Beihang University, Beijing 100191, China; Center of Soft*

https://doi.org/10.1021/acs.langmuir.2c02088
Langmuir 2022, 38, 13880−13887

Matter Physics and Its Applications, Beihang University, Beijing 100191, China; orcid.org/0000-0003-4322-244X; Email: ye.xu@buaa.edu.cn

Authors

Zhaoxia Niu − *School of Mechanical Engineering and Automation, Beihang University, Beijing 100191, China; Center of Soft Matter Physics and Its Applications, Beihang University, Beijing 100191, China;* orcid.org/0000-0003-1139-5282

Han Gao − *School of Mechanical Engineering and Automation, Beihang University, Beijing 100191, China*

Masao Doi − *Center of Soft Matter Physics and Its Applications, Beihang University, Beijing 100191, China; Wenzhou Institute, University of Chinese Academy of Science, Wenzhou, Zhejiang 325000, China*

Jiajia Zhou − *South China Advanced Institute for Soft Matter Science and Technology, School of Emergent Soft Matter, South China University of Technology, Guangzhou 510640, China; Guangdong Provincial Key Laboratory of Functional and Intelligent Hybrid Materials and Devices, South China University of Technology, Guangzhou 510640, China;* orcid.org/0000-0002-2258-6757

Complete contact information is available at: https://pubs.acs.org/10.1021/acs.langmuir.2c02088

Notes

The authors declare no competing financial interest.

■ ACKNOWLEDGMENTS

This work is supported by the National Natural Science Foundation of China (NSFC 11674019 and 12072010) and the Fundamental Research Funds for the Central Universities (YWF-22-K-101).

■ REFERENCES

(1) Chambers, L. D.; Stokes, K. R.; Walsh, F. C.; Wood, R. J. K. Modern Approaches to Marine Antifouling Coatings. *Surf. Coat. Technol.* **2006**, *201*, 3642−3652.

(2) Roberts, C. C.; Francis, L. F. Drying and Cracking of Soft Latex Coatings. *J. Coat. Technol. Res.* **2013**, *10*, 441−451.

(3) Hu, L.; Wu, H.; La Mantia, F.; Yang, Y.; Cui, Y. Thin, Flexible Secondary Li-Ion Paper Batteries. *ACS Nano* **2010**, *4*, 5843−5848.

(4) Colvin, V. L. From Opals to Optics: Colloidal Photonic Crystals. *MRS Bull.* **2001**, *26*, 637−641.

(5) Vlasov, Y. A.; Bo, X.-Z.; Sturm, J. C.; Norris, D. J. On-Chip Natural Assembly of Silicon Photonic Bandgap Crystals. *Nature* **2001**, *414*, 289−293.

(6) Lee, W. P.; Routh, A. F. Why Do Drying Films Crack? *Langmuir* **2004**, *20*, 9885−9888.

(7) Tirumkudulu, M. S.; Punati, V. S. Solventborne Polymer Coatings: Drying, Film Formation, Stress Evolution, and Failure. *Langmuir* **2022**, *38*, 2409−2414.

(8) Pauchard, L.; Parisse, F.; Allain, C. Influence of Salt Content on Crack Patterns Formed through Colloidal Suspension Desiccation. *Phys. Rev. E: Stat. Phys., Plasmas, Fluids, Relat. Interdiscip. Top.* **1999**, *59*, 3737−3740.

(9) Pauchard, L.; Adda-Bedia, M.; Allain, C.; Couder, Y. Morphologies Resulting from the Directional Propagation of Fractures. *Phys. Rev. E: Stat. Phys., Plasmas, Fluids, Relat. Interdiscip. Top.* **2003**, *67*, 027103.

(10) Goehring, L.; Clegg, W. J.; Routh, A. F. Wavy Cracks in Drying Colloidal Films. *Soft Matter* **2011**, *7*, 7984−7987.

(11) Lazarus, V.; Pauchard, L. From Craquelures to Spiral Crack Patterns: Influence of Layer Thickness on the Crack Patterns Induced by Desiccation. *Soft Matter* **2011**, *7*, 2552−2559.

(12) Han, W.; Li, B.; Lin, Z. Drying-Mediated Assembly of Colloidal Nanoparticles into Large-Scale Microchannels. *ACS Nano* **2013**, *7*, 6079−6085.

(13) Dufresne, E. R.; Corwin, E. I.; Greenblatt, N. A.; Ashmore, J.; Wang, D. Y.; Dinsmore, A. D.; Cheng, J. X.; Xie, X. S.; Hutchinson, J. W.; Weitz, D. A. Flow and Fracture in Drying Nanoparticle Suspensions. *Phys. Rev. Lett.* **2003**, *91*, 224501.

(14) Keddie, J. L. Film Formation of Latex. *Mater. Sci. Eng., R* **1997**, *21*, 101−170.

(15) Almanza-Workman, A. M.; Taussig, C. P.; Jeans, A. H.; Cobene, R. L. Fabrication of Three-Dimensional Imprint Lithography Templates by Colloidal Dispersions. *J. Mater. Chem.* **2011**, *21*, 14185−14192.

(16) Wohlleben, W.; Bartels, F. W.; Altmann, S.; Leyrer, R. J. Mechano-Optical Octave-Tunable Elastic Colloidal Crystals Made from Core−Shell Polymer Beads with Self-Assembly Techniques. *Langmuir* **2007**, *23*, 2961−2969.

(17) Limousin, E.; Ballard, N.; Asua, J. M. Soft Core−Hard Shell Latex Particles for Mechanically Strong VOC-Free Polymer Films. *J. Appl. Polym. Sci.* **2019**, *136*, 47608.

(18) Lewis, J. A. Colloidal Processing of Ceramics. *J. Am. Ceram. Soc.* **2000**, *83*, 2341−2359.

(19) Procházka, J.; Kavan, L.; Zukalová, M.; Frank, O.; Kalbáč, M.; Zukal, A.; Klementová, M.; Carbone, D.; Graetzel, M. Novel Synthesis of the TiO2(B) Multilayer Templated Films. *Chem. Mater.* **2009**, *21*, 1457−1464.

(20) Prosser, J. H.; Brugarolas, T.; Lee, S.; Nolte, A. J.; Lee, D. Avoiding Cracks in Nanoparticle Films. *Nano Lett.* **2012**, *12*, 5287−5291.

(21) Muzzillo, C. P.; Reese, M. O.; Mansfield, L. M. Fundamentals of Using Cracked Film Lithography to Pattern Transparent Conductive Metal Grids for Photovoltaics. *Langmuir* **2020**, *36*, 4630−4636.

(22) Xie, J.; Guo, J.; Wang, D.; Cang, Y.; Zhang, W.; Zhou, J.; Peng, B.; Li, Y.; Cui, J.; Chen, L.; Fytas, G.; Deng, X. Self-Assembly of Colloidal Nanoparticles into Well-Ordered Centimeter-Long Rods via Crack Engineering. *Adv. Mater. Interfaces* **2021**, *8*, 2000222.

(23) Pan, S.; Zou, H.; Wang, A. C.; Wang, Z.; Yu, J.; Lan, C.; Liu, Q.; Wang, Z. L.; Lian, T.; Peng, J.; Lin, Z. Rapid Capillary-Assisted Solution Printing of Perovskite Nanowire Arrays Enables Scalable Production of Photodetectors. *Angew. Chem. Int. Ed.* **2020**, *59*, 14942−14949.

(24) Ermis, M.; Akkaynak, D.; Chen, P.; Demirci, U.; Hasirci, V. A High Throughput Approach for Analysis of Cell Nuclear Deformability at Single Cell Level. *Sci. Rep.* **2016**, *6*, 36917.

(25) Ermis, M.; Antmen, E.; Hasirci, V. Micro and Nanofabrication Methods to Control Cell-Substrate Interactions and Cell Behavior: A Review from the Tissue Engineering Perspective. *Bioact. Mater.* **2018**, *3*, 355−369.

(26) Kim, C.-S.; Ahn, S.-H.; Jang, D.-Y. Review: Developments in Micro/Nanoscale Fabrication by Focused Ion Beams. *Vacuum* **2012**, *86*, 1014−1035.

(27) Ariga, K.; Minami, K.; Ebara, M.; Nakanishi, J. What Are the Emerging Concepts and Challenges in NANO? Nanoarchitectonics, Hand-Operating Nanotechnology and Mechanobiology. *Polym. J.* **2016**, *48*, 371−389.

(28) Routh, A. F. Drying of Thin Colloidal Films. *Rep. Prog. Phys.* **2013**, *76*, 046603.

(29) Lei, H.; Francis, L. F.; Gerberich, W. W.; Scriven, L. E. Stress Development in Drying Coatings after Solidification. *AIChE J.* **2002**, *48*, 437−451.

(30) Boulogne, F.; Pauchard, L.; Giorgiutti-Dauphiné, F.; Botet, R.; Schweins, R.; Sztucki, M.; Li, J.; Cabane, B.; Goehring, L. Structural Anisotropy of Directionally Dried Colloids. *Europhys. Lett.* **2014**, *105*, 38005.

(31) Lama, H.; Gogoi, T.; Basavaraj, M. G.; Pauchard, L.; Satapathy, D. K. Synergy between the Crack Pattern and Substrate Elasticity in

Colloidal Deposits. *Phys. Rev. E: Stat. Phys., Plasmas, Fluids, Relat. Interdiscip. Top.* **2021**, *103*, 032602.
(32) Dufresne, E. R.; Stark, D. J.; Greenblatt, N. A.; Cheng, J. X.; Hutchinson, J. W.; Mahadevan, L.; Weitz, D. A. Dynamics of Fracture in Drying Suspensions. *Langmuir* **2006**, *22*, 7144−7147.
(33) Inasawa, S.; Yamaguchi, Y. Self-Organized Pattern Formation of Cracks Perpendicular to the Drying Direction of a Colloidal Suspension. *Soft Matter* **2012**, *8*, 2416−2422.
(34) Goehring, L.; Li, J.; Kiatkirakajorn, P. C. Drying Paint: From Micro-Scale Dynamics to Mechanical Instabilities. *Philos. Trans. R. Soc., A* **2017**, *375*, 20160161.
(35) Jagla, E. A. Stable Propagation of an Ordered Array of Cracks during Directional Drying. *Phys. Rev. E: Stat. Phys., Plasmas, Fluids, Relat. Interdiscip. Top.* **2002**, *65*, 046147.
(36) Giorgiutti-Dauphiné, F.; Pauchard, L. Elapsed Time for Crack Formation during Drying. *Eur. Phys. J. E* **2014**, *37*, 39.
(37) Li, B.; Valverde, L. R.; Zhang, F.; Zhou, Y.; Li, S.; Diao, Y.; Wilson, W. L.; Schroeder, C. M. Macroscopic Alignment and Assembly of π-Conjugated Oligopeptides Using Colloidal Microchannels. *ACS Appl. Mater. Interfaces* **2017**, *9*, 41586−41593.

https://doi.org/10.1021/acs.langmuir.2c02088
Langmuir 2022, 38, 13880−13887

Supplementary Information：

Interplay of consolidation fronts and cracks in drying colloidal coatings and its application in controlling crack pattern formation

Zhaoxia Niu,[1,2] Han Gao,[2] Masao Doi,[1,3] Jiajia Zhou,[4,5] Ye Xu[1,2,*]

[1]*School of Mechanical Engineering and Automation, Beihang University, Beijing 100191, China;*

[2]*Center of Soft Matter Physics and Its Applications, Beihang University, Beijing 100191, China;*

[3]*Wenzhou Institute, University of Chinese Academy of Science, Wenzhou, Zhejiang 325000, China;*

[4] *South China Advanced Institute for Soft Matter Science and Technology, School of Emergent Soft Matter, South China University of Technology, Guangzhou 510640, China;*

[5]*Guangdong Provincial Key Laboratory of Functional and Intelligent Hybrid Materials and Devices, South China University of Technology, Guangzhou 510640, China*

1. Supplementary Movies

MovieS1: Time-lapse fluorescent images of consolidation fronts and cracks in directional drying channels with drying edge of angle $\theta = 60°$. The movie is accelerated by 240 times.

MovieS2: Time-lapse fluorescent images of consolidation fronts and cracks in directional drying channels with drying edge of angle $\theta = 90°$. The movie is accelerated by 240 times.

MovieS3: Time-lapse fluorescent images of consolidation fronts and cracks in directional drying channels with drying edge of angle $\theta = 120°$. The movie is accelerated by 240 times.

MovieS4: Time-lapse fluorescent images recorded during the formation of wavy cracks in directional drying channels with alternating temperature gradients. The movie is accelerated by 480 times.

1. Supplementary Figures

Colloidal suspension

The size distribution from the DLS (dynamic light scattering) of the aqueous suspensions of monodisperse colloidal silica nanoparticles (~0.3vt%) is shown in the Fig. S1(a). The morphology and particle size can be obtain from TEM and SEM, as shown in the Fig.S1(b-e).

To facilitate the visualization of consolidation fronts, we added a slight number of 0.1μm fluorescent particles into the silica colloidal suspension at the number ratio between them of approximately 1:10000. In order to exclude the effect of fluorescent particles on the crack patterns, we observe the crack pattern in the colloidal particle coatings with and without the fluorescent

particles. In the colloidal coatings containing fluorescent particles, the volume fraction of the fluorescent particles is about 0.2%. The crack patterns in both cases are shown in Fig.S2. All experiments were performed under the same evaporation conditions (about 22℃,50%RH). The results show that the crack patterns with and without fluorescent particles have similar morphology. The addition of the fluorescent particle in the colloidal silica suspension has no visible effect on the crack patterns.

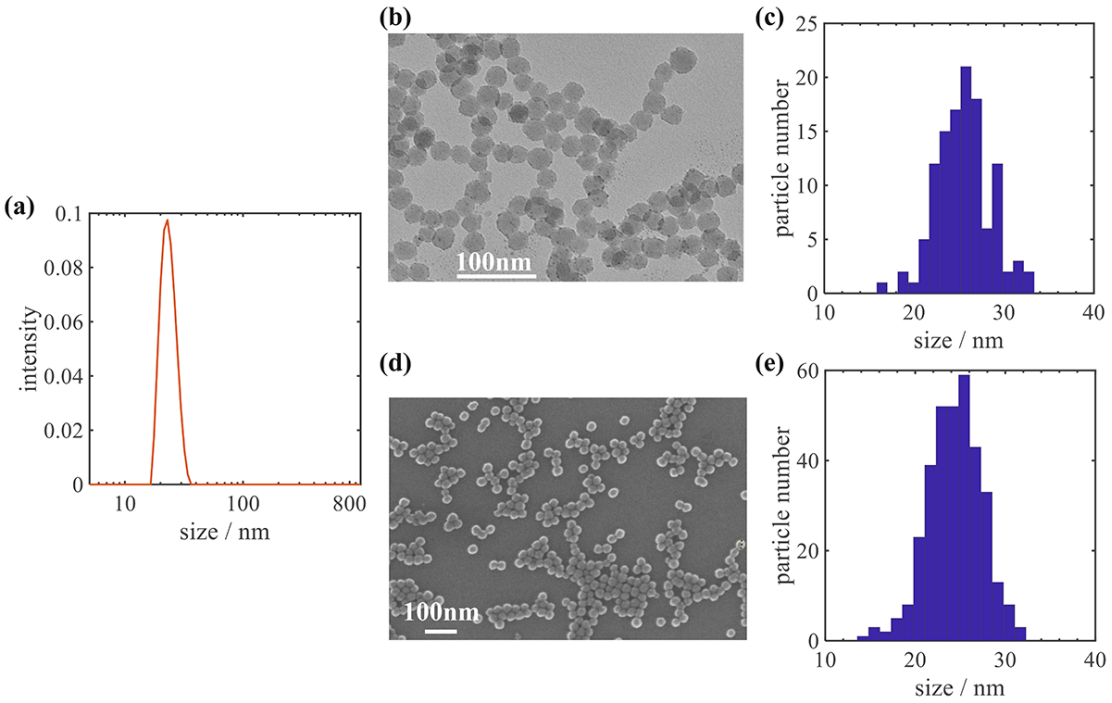

Figure S1: *Particle size distributions, TEM and SEM micrographs of silica.* (a) particle size distribution from dynamic light scattering (DLS). The average of the particle size and standard deviation are 23nm and 3nm, respectively. (b) TEM micrograph. (c) Particle size distribution from the TEM micrograph. The average and the standard deviation are 26nm and 3nm, respectively. (d) SEM micrograph. (e) Particle size distribution from the SEM micrograph. The average and the standard deviation are 24nm and 3nm, respectively.

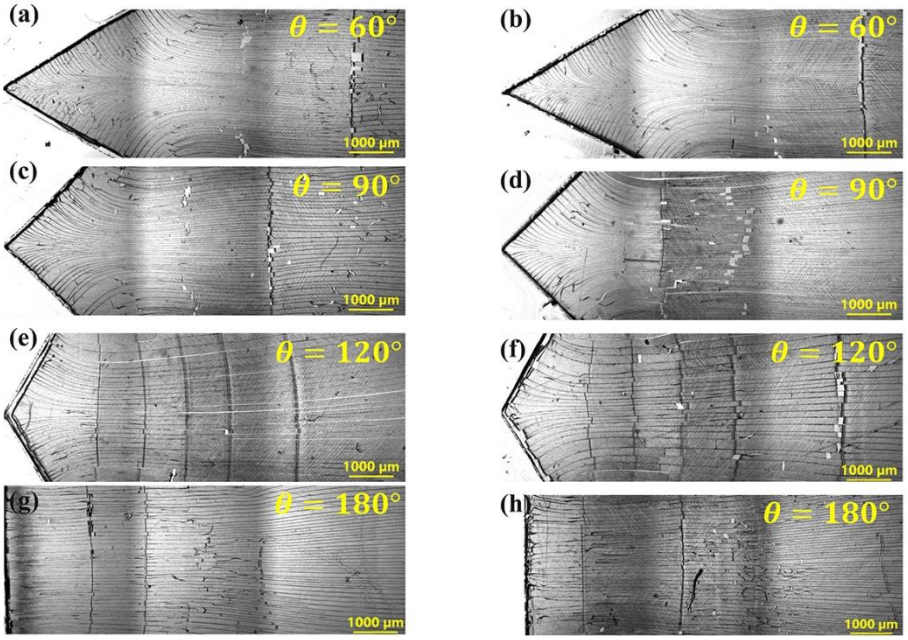

Figure S2: *Comparison of crack patterns in the particle coatings with and without florescent particles.* (a), (c), (e) and (g): White light microscopy images of colloidal particle coating with fluorescent particles in directional drying setups with drying edges of angel $\theta = 60°, \theta = 90°, \theta = 120°$ and $\theta = 180°$, respectively. (b), (d), (f) and (h): White light microscopy images of colloidal particle coating without fluorescent particles in directional drying setups with drying edges of angel $\theta = 60°, \theta = 90°, \theta = 120°$ and $\theta = 180°$, respectively.

Morphology of consolidation fronts and cracks

To display the curvature of the consolidation fronts and cracks in channels of different angled drying edges, the maximum curvature is given in Fig. S3. The maximum curvature is calculated by averaging five percent of the high curvature data. The result shows that the maximum curvature of consolidation fronts and crack patterns decreases as decreasing of the angle of drying edge.

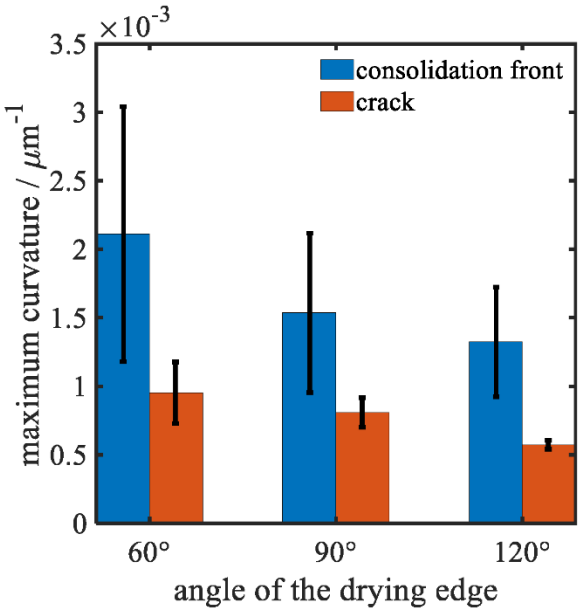

Figure S3: *Maximum curvature of consolidation fronts and cracks in drying setups with different angled drying edge.* Blue bar represents the maximum curvature of consolidation fronts and the orange color bar represents maximum curvature of cracks.

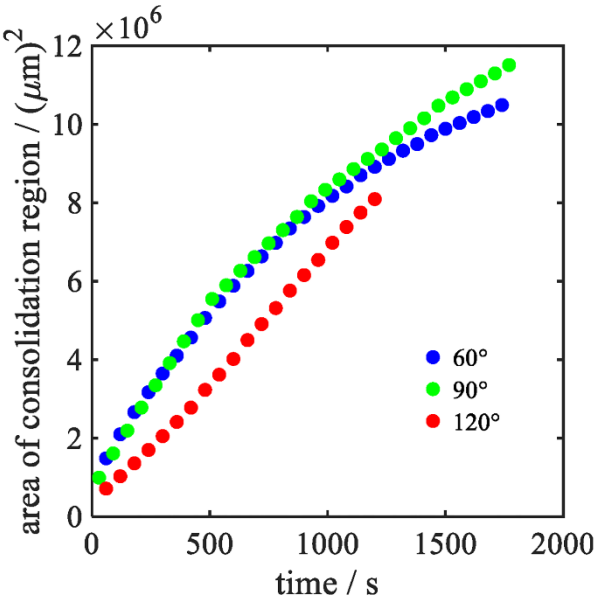

Figure S4: *The area evolution of the consolidation region over time.* The blue, green, and red dots represent the evolution relationship in the drying setups with drying edge angle of $\theta = 60°$, $\theta = 90°$ and $\theta = 120°$, respectively. The consolidation region is meaning the region between the drying edge and the consolidation front.The slopes of the three curves meaning the evolution rate of the area of consolidation region over time are $7.28 \times 10^{-3} \mu m^2/s$, $7.96 \times 10^{-3} \mu m^2/s$, and $6.67 \times 10^{-3} \mu m^2/s$ respectively

Geometrical relation between the crack growth direction and consolidation fronts.

The deviations between the cross angles γ and 90° and the local crack curvature along a single crack can further confirm the slight deviation of the cross angles for cracks with high curvatures. The absolute value of the deviation of cross angles from 90° ($\delta = |\gamma - 90°|$) and the curvature along a single crack with the length of the crack growth with drying edge angle of θ=60°, θ=90° and θ=120° are shown in Fig.S5-S7, respectively. These plots show that the deviation δ and the local crack curvature with the length of crack growth display the same trend, which can confirm

the phenomenon that the slight deviation between the cracks and the direction perpendicular to the consolidation fronts appear to increase when the curved cracks form.

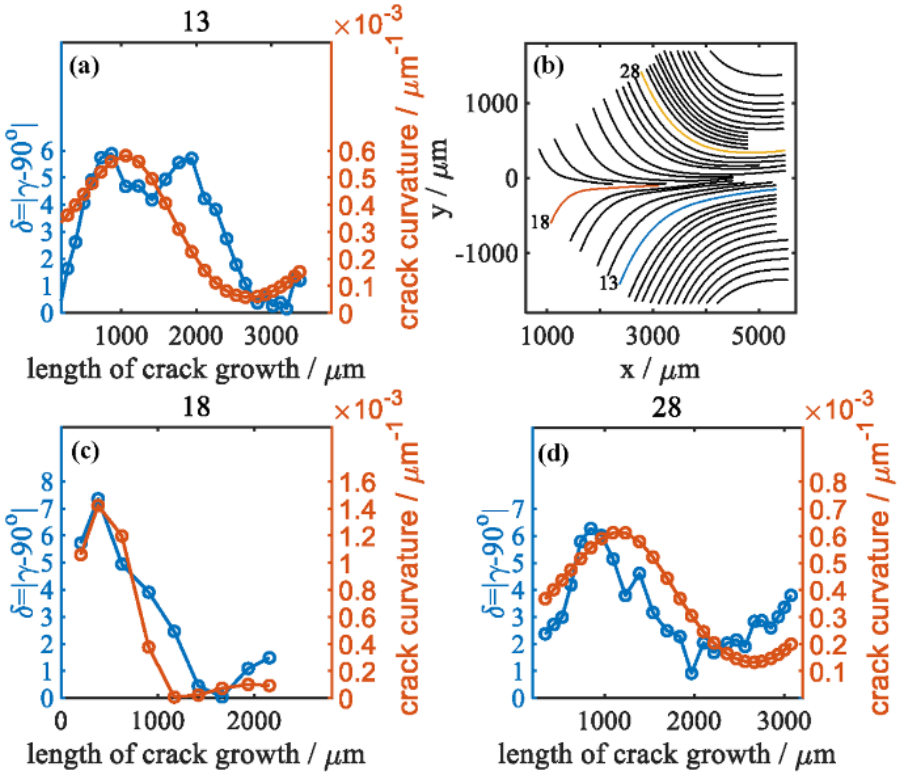

Figure S5: *The evolution of deviation δ and the local curvature versus the length of crack propagation for a single crack with drying edge angle θ=60°.* (a)(c)(d) The evolution of the deviation $\delta = |\gamma - 90°|$ with the length of crack growth (blue curve) and the evolution of crack curvature with the length of crack growth (orange curve). The number on the top of the plot represents the corresponding crack in the plot (b). (b) The label numbers of cracks with edge angles of 60°.

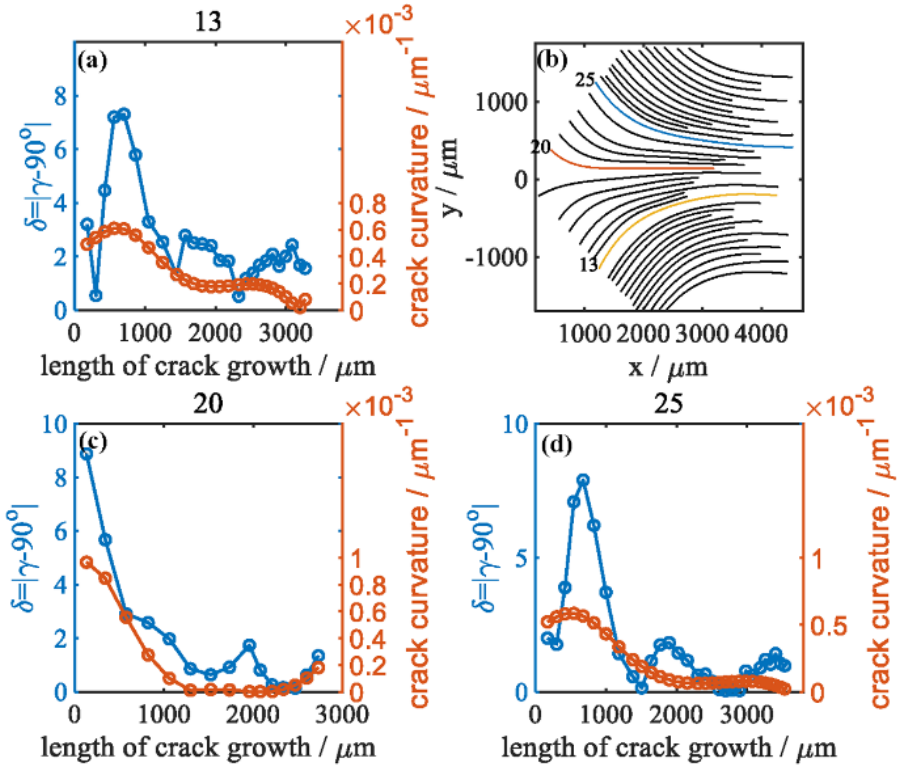

Figure S6: *The evolution of deviation δ and the local curvature versus the length of crack propagation for a single crack with drying edge angle θ=90°.* (a)(c)(d) The evolution of the deviation $\delta = |\gamma - 90°|$ with the length of crack growth (blue curve) and the evolution of crack curvature with the length of crack growth (orange curve). The number on the top of the plot represents the corresponding crack in the plot (b). (b) The label numbers of cracks with edge angles of 90°.

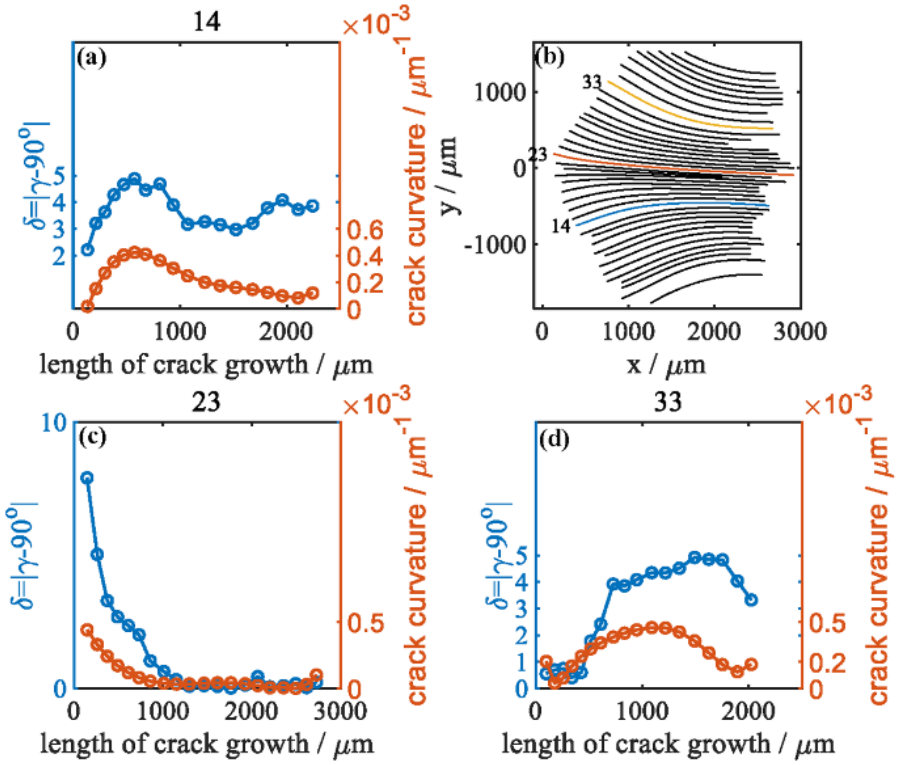

Figure S7: *The evolution of deviation δ and the local curvature versus the length of crack propagation for a single crack with drying edge angle θ=120°.* (a)(c)(d) The changes of the deviation $\delta = |\gamma - 90°|$ with the length of crack propagation (blue curve) and the changes of crack curvature with the length of crack propagation (orange curve). The number on the top of the plot represents the corresponding crack in the plot (b). (b) The label numbers of cracks with edge angles of 120°.

Guiding crack growth direction by controlling advancing consolidation fronts

The statistical results of cross angles γ between the growth direction of the crack and the tangent of the consolidation fronts in a channel with flat drying edge under uniform temperature field and gradient temperature field is shown in Fig. S8. The result shows a much narrower distribution than the cross angles in the channel with angled drying edge. The curves are fitted to a Gaussian distribution. The average of cross angles under

uniform temperature field is about 88.22° with the standard deviation 4.67° and the average of cross angles under gradient temperature field is $89.20 \pm 0.3°$ with the standard deviation is $2.19 \pm 0.5°$. The result shows that the cracks tend to grow along the direction perpendicular to the consolidation front whether under the uniform or gradient temperature field. Therefore, the growth of cracks can be guided by consolidation fronts. The evolution process of the consolidation front morphology under gradient temperature field is shown in Fig.S9. The evolution morphology of the advancing consolidation front keeps stable after about three minutes. When the direction of the temperature gradient field changes, the deflection morphology of consolidation fronts changes and the cracks deflect upwards.

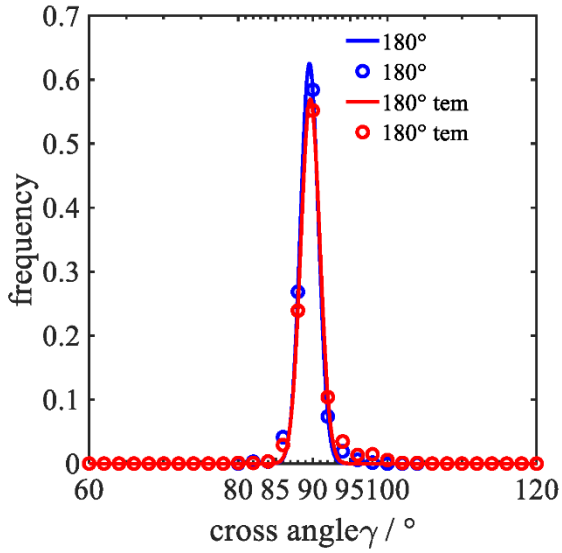

Figure S8: *The statistical frequency of cross angles between consolidation fronts and cracks under uniform (blue) and gradient temperature gradient field (red).* Scatter points represent the experiment data and the line shows the fitting of Gaussian distribution.

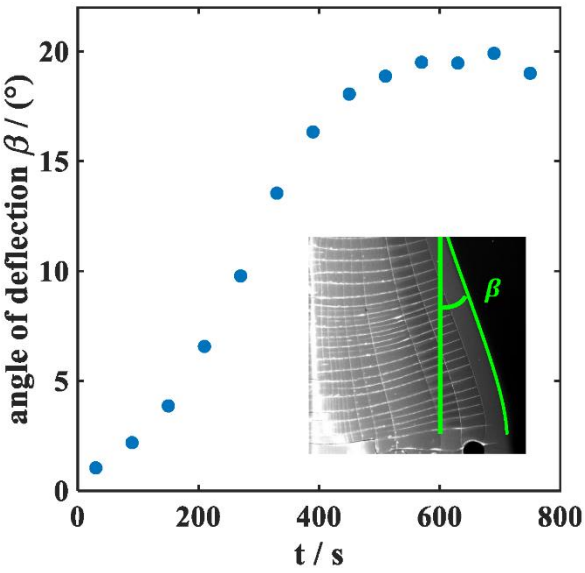

Figure S9: *The deflection angle of consolidation front at different drying time.* The inset indicates the deflection angle of consolidation front.

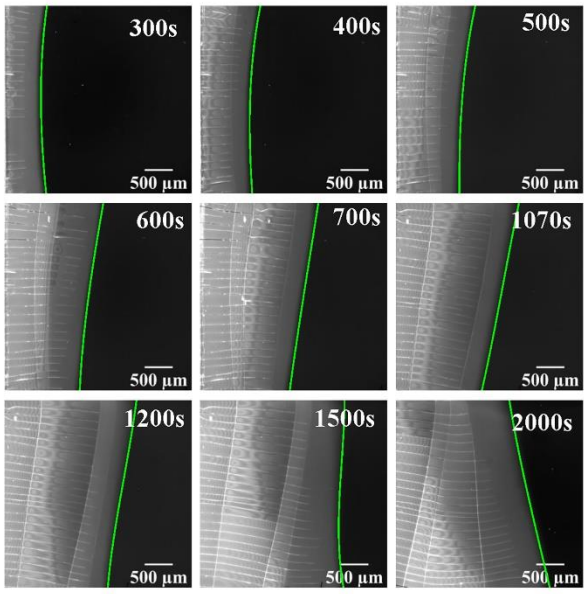

Figure S10: *The evolution process of the consolidation front morphology under gradient temperature field at different time.* The green line represents the consolidation front.